

Claycode: Stylable and Deformable 2D Scannable Codes

MARCO MAIDA, Independent Researcher, United Kingdom
 ALBERTO CRESCINI, Independent Researcher, United Kingdom
 MARCO PERRONET, Independent Researcher, United Kingdom
 ELENA CAMUFFO, Independent Researcher, Italy



Fig. 1. Examples of Claycodes using different shapes and styles. From the left: “space”, “👁️”, “hello”, “magic”.

This paper introduces Claycode, a novel 2D scannable code designed for extensive stylization and deformation. Unlike traditional matrix-based codes (e.g., QR codes), Claycodes encode their message in a tree structure. During the encoding process, bits are mapped into a topology tree, which is then depicted as a nesting of color regions drawn within the boundaries of a target polygon shape. When decoding, Claycodes are extracted and interpreted in real-time from a camera stream. We detail the end-to-end pipeline and show that Claycodes allow for extensive stylization without compromising their functionality. We then empirically demonstrate Claycode’s high tolerance to heavy deformations, outperforming traditional 2D scannable codes in scenarios where they typically fail.

CCS Concepts: • **Human-centered computing** → **Interaction paradigms**; **Accessibility technologies**; • **Computing methodologies** → **Image processing**; • **Information systems** → **Multimedia content creation**; • **Theory of computation** → **Computational geometry**.

Additional Key Words and Phrases: Topological Encoding, 2D Scannable codes, Stylization, Topology Optimization

ACM Reference Format:

Marco Maida, Alberto Crescini, Marco Perronet, and Elena Camuffo. 2025. Claycode: Stylable and Deformable 2D Scannable Codes. *ACM Trans. Graph.* 44, 4 (August 2025), 14 pages. <https://doi.org/10.1145/3730853>

1 Introduction

With the large adoption of smartphones, 2D scannable codes (such as QR codes [Tiwari 2016]) have transcended the industrial domain

Authors’ Contact Information: Marco Maida, Independent Researcher, London, United Kingdom, mmaidacs@gmail.com; Alberto Crescini, Independent Researcher, London, United Kingdom, info@alberto.fun; Marco Perronet, Independent Researcher, London, United Kingdom, perronet.marco@gmail.com; Elena Camuffo, Independent Researcher, Padova, Italy, elenacamuffo97@gmail.com.

Copyright held by the owner/author(s). This is the author’s version of the work. It is posted here for your personal use. Not for redistribution. The definitive Version of Record was published in “ACM Transactions on Graphics (Proc. SIGGRAPH 2025)”.
 © 2025 Copyright held by the owner/author(s).
 ACM 1557-7368/2025/8-ART
<https://doi.org/10.1145/3730853>

and become a part of everyday life. Scannable codes are ubiquitous in ticketing, mobile payments, advertising, as gateways to digital experiences in museums and cultural institutions, and augmented reality applications [Ozkaya et al. 2015]. While QR codes and other barcodes have proven highly efficient at pictorially encoding information, their design often lacks aesthetic appeal. Constrained by strict algorithmic requirements, they often look out of place on otherwise carefully designed posters and artworks. Over the years, the demand for visual adaptability has grown significantly, leading to custom-branded codes like Spotify Codes [Spotify 2017] and App Clips [Apple 2020], businesses that provide styled QR codes to corporations and individuals [Flowcode 2024; QRCode AI 2024], and codes purpose-built for the visually impaired [de Alicante 2016]. In this work, we introduce Claycodes, two-dimensional scannable codes that can be styled and significantly deformed, making it possible to embed a message in an artwork in a visually pleasing way. The high deformability of Claycodes allows them to remain scannable on elastic surfaces, like textiles and skin tissue [Wan et al. 2023], and deformations induced by a large scanning angle [Kurniawan et al. 2019]. Moreover, unlike traditional scannable codes, Claycodes are not confined to a predefined shape, making them ideal for embedding within shape-constrained spaces like electrical components.

Claycodes are the first *topological codes*: they embed a message within the tree structure defined by the topology of its color regions. Several other works explored the use of topology as a mean to build visual markers [Costanza and Huang 2009; Getschmann and Ehtler 2021; Yu et al. 2020], but Claycodes are the first fully functional topological codes able to carry an arbitrary bit payload.

This paper details the end-to-end pipeline of Claycodes (fig. 2) starting from section 3, where we devise a bidirectional mapping between bit strings and trees optimized to produce readable codes. In section 4, we show how to render the resulting trees within a target polygon, ultimately producing a Claycode. Finally, in section 5 we outline the process of detecting and decoding Claycodes

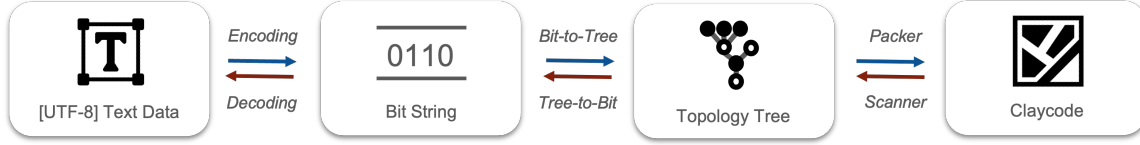


Fig. 2. The encoding and decoding pipeline of Claycodes.

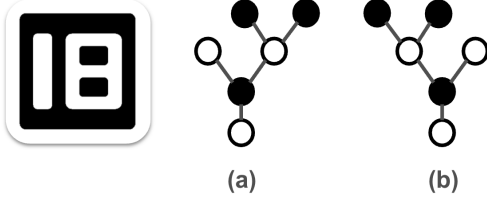


Fig. 3. Isomorphic trees map to the same Claycode.

from a camera stream in real-time, and discuss error detection and redundancy techniques. We conclude with section 6, where we empirically demonstrate the resistance of Claycodes to deformations and stylization by conducting a comparative scanning test between our implementation of Claycodes, QR Codes, and Code-128 Barcodes [ISO 2007].

2 Related Work

QR-Codes [Tiwari 2016] receive large interest from the academic community. Earlier attempts to embed images in QR-Codes focus on deforming [Chu et al. 2013] or re-shuffling [Cox 2012; Xu et al. 2021] the codes' modules to approximate the target image, while minimizing the error introduced. More recent advancements, based on neural techniques, have dramatically improved the quality of image-embedded QR Codes. Notably, [Xu et al. 2019] pioneered the use of Neural Style Transfer to QR Codes, a method further refined by ArtCoder [Su et al. 2021], and then evolved into diffusion techniques, such as GladCoder [Xie et al. 2024]. A common theme in these works is the balance between visual quality and robustness, sometimes biasing the generators with saliency maps [Lin et al. 2015, 2013] to the parts of the image visually considered important. All of the cited techniques generally damage the code to some degree. Other works propose codes purpose-built to be styled: PiCodes [Chen et al. 2016] are generated from an input image, and its pixel intensities carry the message. Several other systems explore visual or structural embedding strategies that preserve, rather than compromise, the overall appearance of the carrier. Notably, StructCode [Dogan et al. 2023a] encodes bits directly in the geometric features of laser-cut objects, offering an unobtrusive and aesthetically aligned approach. Related examples include FontCode [Xiao et al. 2018], BrightMarker [Dogan et al. 2023b], and Imprinto [Feick et al. 2025].

To the best of our knowledge, Claycodes are the first topological 2D scannable codes that can carry arbitrary bit sequences. However, the literature contains several works on topological *fiducial markers*, pioneered by D-Touch [Costanza and Huang 2009; Costanza et al. 2003] and followed by ReacTIVision [Bencina and Kaltenbrunner

2005], ARTag [Fiala 2004], ARTcodes [Yang et al. 2016], TopoTag [Yu et al. 2020], and Seedmarkers [Getschmann and Ehtler 2021]. Fiducial markers are popular in augmented reality applications, but their visual rigidity often detracts from the immersive experience. ARTTag [Higashino et al. 2016], is a recent example of stylable fiducial marker, designed around pairs of circles that can blend into an artwork. Claycode builds on the foundations laid by the aforementioned work, evolving the topological approach to 2D codes. Along this direction, Jung et al. [Jung et al. 2019; Jung and Vogel 2018] propose human-designable visual markers that combine structure and stylistic freedom, supporting intentional design and fine control over appearance.

By contrast, a separate line of work focuses on invisibility or machine-only readability. Examples include AirCode [Li et al. 2017], LayerCode [Maia et al. 2019], StegaStamp [Tancik et al. 2020], and again InfraredTags [Dogan et al. 2022], which rely on materials or wavelengths not visible to the human eye. These methods fall more squarely into steganography or optical tracking, and while technologically adjacent, they differ in goal: hiding or isolating the code from human perception, rather than integrating it visually as Claycode does.

3 Bit-Tree Encoding

We begin by introducing Claycode's *bit-tree encoding*, a bidirectional mapping between the set of bit strings $\{0, 1\}^*$ and trees. Throughout this paper, we work with *rooted, unlabeled, ordered trees*, i.e., directed acyclic graphs where there is a single distinguished node with no incoming edges called *root*, and every other node has exactly one incoming edge – its *parent*. T may refer to either a tree $T \in \mathcal{T}$ or its root node, depending on the context. Nodes sharing the same parent are referred to as *siblings*. The order among siblings is significant: given a parent node T , we indicate its ordered children with a duplicate-free list $C(T) = [T_1, T_2, \dots]$. If $C(T) = []$, then T is a *leaf*. A node $T \neq T'$ is a *descendant* of T' if there exists a path from T' to T . We call $D(T)$ the set of all descendants of T . Finally, two trees $T, T' \in \mathcal{T}$ are *isomorphic* ($T \sim T'$) if one can be transformed into the other via a sequence of permutations of siblings.

A *bit-tree encoding* is a pair of functions (f, g) such that:

$$\begin{aligned} f : \{0, 1\}^* &\rightarrow \mathcal{T}, & g : \mathcal{T} &\rightarrow \{0, 1\}^*, \\ g(f(b)) &= b \quad \forall b \in \{0, 1\}^* \\ T \sim T' &\implies g(T) = g(T'), \quad \forall T, T' \in \mathcal{T}. \end{aligned} \quad (1)$$

The last line of eq. (1) is needed as Claycodes have no way of visually encoding sibling's ordering (fig. 3). We hence define an encoding that yields the same message when permuting siblings. Defining a pair of functions that formally respects eq. (1) is relatively

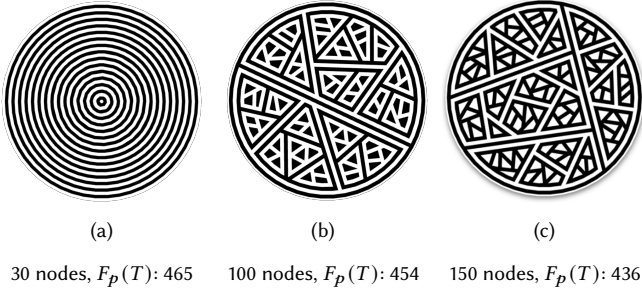


Fig. 4. Shallow trees are more space-efficient.

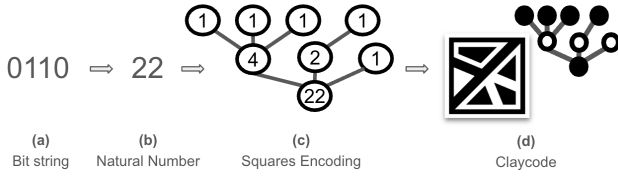


Fig. 5. The Squares bit-tree encoding.

straightforward. However, the bit-tree encoding largely determines the data capacity and readability of Claycodes, and as such, it is subject to a series of additional requirements.

3.1 Bit-Tree Requirements For Space-Efficient Claycodes

An important quality of any encoding is to minimize the size of the encoded message within its target medium. Claycodes pose a challenge in defining what “size” is: despite the number of nodes in the topology tree correlates with the space needed to draw the code, it is not a comprehensive metric by itself. As exemplified in fig. 4, when a topology tree is rendered into a Claycode, each node surrounds all its descendants, which means that each parent node requires more space than its children. Highly nested topologies are thus significantly less space-efficient compared to shallower, more planar configurations. To capture the aforementioned aspects into a metric, we define the *footprint* of a node as:

$$F(T) = 1 + |D(T)| \quad (2)$$

By extension, we further call the *total footprint* of a node the sum of its own footprint plus the one of all its descendants, i.e., $F_t(T) = F(T) + \sum_{T_d \in D(T)} F(T_d)$. The total footprint scales quadratically with the depth of the tree, and linearly with its width. We selected this formulation because of its simplicity and its strong – empirically observed – correlation with the visual complexity of the generated Claycode across different input shapes.

With the footprint metric in place, we define the requirements for Claycode’s bit-tree encoding. Given a bit string b , the first requirement **(R1)** of an effective bit-tree encoding (f, g) is to minimize the total footprint of the generated tree $F_t(f(b))$. Additionally, $F_t(f(b))$ must strongly correlate with the length of b , mapping longer bit strings to trees with larger footprint **(R2)**. Further, many bit-tree encodings suffer from significant size inconsistencies: depending on the specific combination of ones and zeroes in the input bit string b , $F_t(f(b))$ widely varies. Such variability is problematic in Claycodes,

as it creates instances of short input messages requiring disproportionately large amounts of space to be represented. Therefore, $F_t(f(b))$ must have low (positive or negative) correlation with the percentage of ones in the input message **(R3)**. Finally, to the best of our knowledge, existing tree ranking and generation methods are either based on successor functions [Beyer and Hedetniemi 1980; Effantin 2004; Li 1997; Shin-ichi Nakano 2003], requiring to compute $n - 1$ predecessor trees to output the n th one, or prime factorization [Abe 1994; Cappello 1988; Skliar et al. 2020]. Scannable codes typically contain short strips of text, leading to an expected payload of hundreds of bits. Even with a short message of 100 bits, there are 2^{100} possible message combinations, rendering both enumeration and prime factorization-based techniques unfeasible. A bit-tree encoding must be computable on commercial hardware within milliseconds for input messages of hundreds of bits **(R4)**. Guided by **(R1-R4)**, we devise a bit-tree encoding inspired by [Abe 1994].

3.2 The Squares Encoding

First, we modify the problem to work on natural numbers instead of bit strings. We define f' and g' so that:

$$\begin{aligned} f' : \mathbb{N} &\rightarrow \mathcal{T}, & g' : \mathcal{T} &\rightarrow \mathbb{N}, \\ f(b) &= f'(nat(b)) & g(T) &= bits(g'(T)) \end{aligned} \quad (3)$$

The functions $(nat, bits)$ define a bijection between natural numbers and bit strings, which can be easily derived by interpreting the string as a binary number. We define $(nat, bits)$ in appendix A. The inner functions f' and g' are detailed in algorithm 1, while an illustrative example is provided in fig. 5. The encoding function starts from a node T and the input number n , and decomposes n into a sum of squares $1 + n_1^2 + n_2^2 + \dots + n_k^2$. While n is guaranteed to have at least one, and often several squares decompositions [Pollack and Treviño 2018], in our implementation we adopted a greedy strategy that iteratively selects the largest square in the number, i.e., $\lfloor \sqrt{n} \rfloor$. This operation can be easily implemented on arbitrary-precision integers (required by **(R4)**) via a binary search. Next, k siblings $[T_1, T_2, \dots, T_k]$ are generated (one for each member n_i of the decomposition of n), and assigned as children of T . Finally, the procedure is recursively invoked for the pairs $(T_1, n_1), \dots, (T_k, n_k)$. Whenever 1 is given as input number, the algorithm returns. Due to the commutativity of addition, reordering siblings does not change the encoded number, thus respecting eq. (1). Since each number of the decomposition n_i is guaranteed to be strictly smaller than n , the procedure always terminates.

Evaluation against (R1-R4). We measured the footprint performance of three bit-tree encodings in fig. 6. For each bit string length, we generated 9002 samples, of which 6302 by varying the probability of ones from 0 to 1, and 2700 samples with ascending lag-1 autocorrelation (i.e., the probability that adjacent bits are the same) from 0.1 to 0.9. The generated dataset hence contains a mixture of fully random strings and strings with long consecutive sequences of zeros and ones, in light of **(R3)**. We found Abe’s encoding to best satisfy **(R1)**, **(R2)**, and **(R3)**, and hence adopted it as baseline. However, Abe’s bijection is based on prime factorization, thus becoming unfeasible for strings above 40 bits, and violating **(R4)**. Squares

Algorithm 1: The Squares Bit-Tree Encoding

```

1 Procedure SQUARE_DECOMPOSITION( $n$ ):
2    $n \leftarrow n - 1$ ;  $ns \leftarrow []$ 
3   while  $n \neq 0$  do
4     Append  $\lfloor \sqrt{n} \rfloor$  to  $ns$ 
5      $n \leftarrow n - \lfloor \sqrt{n} \rfloor^2$ 
6   return  $ns$ 
7 Procedure NAT_TO_TREE( $T, n$ ): // Implements  $f'$  of eq. (3)
8    $[n_1, n_2, \dots, n_k] \leftarrow \text{SQUARE\_DECOMPOSITION}(n)$ 
9    $[T_1, T_2, \dots, T_k] \leftarrow \text{generate } k \text{ new nodes}$ 
10  foreach  $T_i \in [T_1, T_2, \dots, T_k]$  do
11    NAT_TO_TREE( $T_i, n_i$ )
12   $C(T) \leftarrow [T_1, T_2, \dots, T_k]$  // Update children of  $T$ 
13 Procedure TREE_TO_NAT( $T$ ): // Implements  $g'$  of eq. (3)
14   $[n_1, n_2, \dots, n_k] \leftarrow [\text{TREE\_TO\_NAT}(T_i) \text{ for } T_i \in C(T)]$ 
15  return  $1 + \sum_{n_i \in [n_1, \dots, n_k]} n_i^2$ 

```

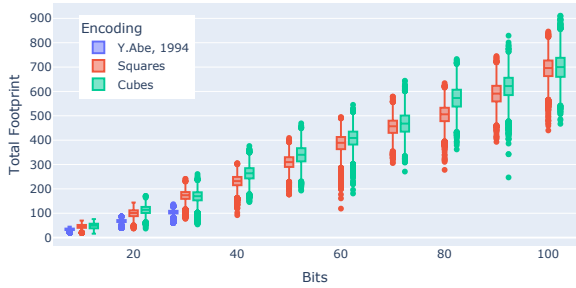


Fig. 6. The total footprint of the Squares, Cubes, and Abe's encoding.

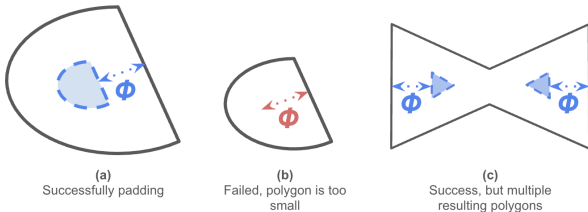


Fig. 7. The three possible outcomes of padding.

has a median footprint 1.34 to 1.67 times larger than Abe's [Abe 1994] encoding, with a standard deviation 1.75 to 2.28 times higher. While the increase is significant, Squares easily scales to thousands of bits, satisfying (R4). Finally, fig. 6 includes *Cubes*, a variation of Squares where the input number is decomposed into a sum of cubes, showcasing it as an example result from various tests we conducted. We evaluated a total of 15 encodings, but excluded most of them from the paper due to space constraints, and ultimately selected Squares for its best overall performance.

4 Packer

The final step of Claycode's encoding pipeline (fig. 2) is the *packer*, the component that renders a given topology tree within an input polygon. The packer is, in one form or another, present in the work

of existing topological markers (e.g., [Bencina and Kaltenbrunner 2005; Costanza and Huang 2009; Yu et al. 2020]). However, Claycodes are not primarily intended to be fiducial markers, but rather to carry bits of payload. They must thus scale well to complex topologies (hundreds of nodes) and support concave shapes. A notable approach in existing literature is Seedmarkers [Getschmann and Echtler 2021], where packing is solved by recursively computing a weighted Voronoi diagram. Although the Seedmarker's approach has the potential to work for Claycode's use case, it is mainly designed for pose estimation (e.g., leaves are always circles), instead of focusing on maximizing the scannability of complex topologies. Moreover, it fails on some highly concave shapes (fig. 8). In the remainder of this section, we detail Claycode's packer, which works on convex and non-convex polygons without self-intersections or holes, and produces scannable Claycodes with thousands of nodes in seconds.

4.1 The Packer Algorithm

The packer, detailed in algorithm 2, takes in input a tree T , a polygon P , and a padding constant ϕ . The algorithm implements a depth-first visit of T , where, at each invocation of the function, a new color region (i.e., node of the topology tree) is drawn. The padding constant ϕ defines the desired minimum thickness of each region. Each packing step applies two *padding* and one *partitioning* operations to P . Padding refers to contracting the boundaries of a polygon, creating a new polygon that is uniformly offset inward from the original. Partitioning means dividing the polygon into non-overlapping sub-polygons. In the following, we aim for the reader to build a visual intuition of the algorithm, and later discuss the padding and partitioning operations. Figure 9 breaks down the packing process for a simple tree. Starting with the square input shape and the root node A , a new region is drawn (fig. 9a) after padding the initial polygon. Then, after the second round of padding, the resulting polygon is partitioned, allocating some space for B and F . The packer assigns more of the available space to B , since it has a larger footprint (recall eq. (2)). The procedure is then recursively invoked, resulting in fig. 9b. Similarly, the polygon associated to B is then partitioned into three polygons, to make space of C , D , and E . Figure 9c is the result of the next three iterations of the algorithm. C , D , and E share a similar amount of space, as they are all leaves. Finally, the packer is invoked for F (fig. 9d), resulting in a completed Claycode.

Note that if ϕ is too large the padding operation can fail, resulting in the failure of the entire procedure. Conversely, partitioning always produces a valid set of polygons. Algorithm 2 heavily depends on the padding and partitioning steps, which we detail next.

4.2 Padding Polygons

We adopt a standard padding implementation (fig. 7) based on [Chen and McMains 2005]. Despite padding has three possible outcomes, we simplify the – rarely observed – scenario of fig. 7c by selecting and returning the polygon with the largest area.

Algorithm 2 receives in input a padding constant ϕ . While ϕ can be tuned to achieve different styles (e.g., a lower ϕ yields larger leaves but thinner color regions for intermediate nodes), we are generally interested in maximizing ϕ to increase the code's readability. To this end, a packing procedure typically involves multiple

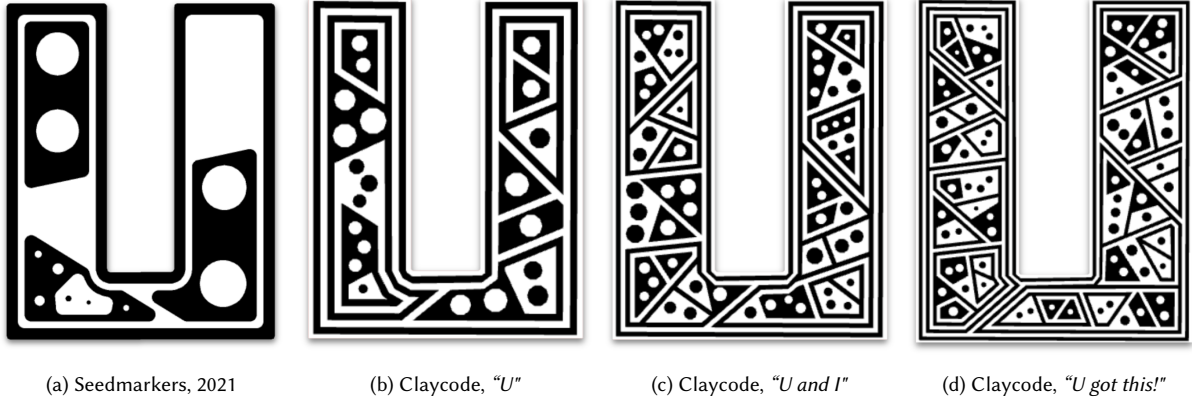


Fig. 8. Claycode's packer when compared to Seedmarkers'.

Algorithm 2: Packing Algorithm: attempt to draw a tree within a given input polygon.

Input: A tree node T , a polygon P , a padding constant $\phi > 0$

Output: SUCCESS if the tree was fully drawn, FAIL otherwise

```

1 Procedure PACK( $T, P, \phi$ ):
2    $P' \leftarrow \text{PAD}(P, \phi/2)$            // Apply first padding
3   if  $P'$  is not valid then return FAIL //  $P$  was too small.
4   Draw  $P'$ 
5    $P'' \leftarrow \text{PAD}(P', \phi/2)$        // Apply second padding
6   if  $P''$  is not valid then return FAIL //  $P'$  was too small.
7    $[P'_1, \dots, P'_k] \leftarrow \text{PARTITION}(P'', C(T))$ 
8   foreach  $T_i \in C(T)$  do
9     if PACK( $T_i, P'_i, \phi$ ) failed then return FAIL
10  return SUCCESS

```

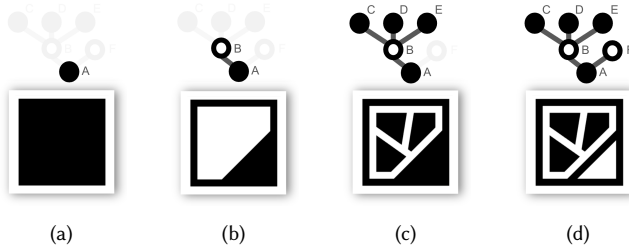


Fig. 9. Packing a tree, whose nodes have been highlighted for illustrative purposes, into a square polygon.

runs of algorithm 2, where a large ϕ is initially selected, and then gradually lowered until packing succeeds – which is more and more likely to happen as ϕ approaches zero. It is important to note that, throughout algorithm 2, ϕ is kept constant, as opposed to dynamically changing whenever the padding operation fails. Varying ϕ is counterproductive, as it produces non-uniformly readable codes.

Finally, each step of algorithm 2 involves two padding operations, which are crucial for two reasons. First, relying on a single padding operation would create uneven thicknesses in intermediate regions: if adjacent polygons were padded independently by ϕ , the resulting

distance between them would be of 2ϕ , creating inconsistencies. Second, the additional padding round of algorithm 2 is applied also in the case of leaf nodes. While P'' is not used in that case, the procedure still terminates if padding fails. This effectively enforces a minimum thickness of ϕ for leaf regions.

4.3 Partitioning polygons

Partitioning takes as input a polygon P and a list of sibling nodes $[T_1, T_2, \dots, T_k]$, and returns a list of polygons $[P_1, P_2, \dots, P_k]$ such that $\bigcup_{i=1}^k P_i = P \wedge \bigcap_{i=1}^k P_i = \emptyset$. We call $\mathcal{P}(P)$ the set of all possible partitions of P . Finding the optimal partitioning is a polygon decomposition problem [Mark Keil 2000] where we aim to distribute the polygon's area to the sibling nodes in a way that increases scannability. We capture the packer's requirements with two principles:

- (1) **Area Proportionality:** The area of each sub-polygon $A(P_i)$ should be proportional to the footprint of each sibling $F(T_i)$. We define the optimal area occupied by the polygon P_i associated with a sibling T_i as:

$$A^*(P_i) = A(P) \cdot \frac{F(T_i)}{\sum_{j=1}^k F(T_j)} \quad (4)$$

- (2) **Circularity Maximization:** To improve readability, Polygons must avoid irregularities or elongations. We evaluate the quality of a polygon with its *circularity* [Cox 1927], which peaks at 1 for a perfect circle and approaches zero for polygons with a disproportionately large perimeter relative to their area. The circularity R of a polygon P is defined as:

$$R(P) = 4\pi \frac{A(P)}{L(P)^2} \quad (5)$$

where $L(P)$ is the perimeter of P .

A visual example of these two principles at work is given in fig. 12. Naturally, most times circularity and area proportionality conflict with each other, so they must be weighted into a single function, resulting in the following minimization problem:

$$\min_{[P_1, \dots, P_k] \in \mathcal{P}} \sum_{i=1}^k \alpha |A(P_i) - A^*(P_i)| + (1 - \alpha) (1 - R(P_i)) \quad (6)$$

Algorithm 3: Searching for a cut (P_1, P_2) of P such that the area of P_1 is close to $A(P) \cdot w_1$ and both P_1 and P_2 have good circularity.

Input: A polygon P and a percentage $w_1 \in (0, 1)$
Output: Two polygons P_1 and P_2

```

1 Procedure POLYGON_CUT( $P, w_1$ ):
2    $best\_error \leftarrow \infty$ 
3    $best\_cut \leftarrow \emptyset$ 
4   while not converged do
5      $P_1, P_2 \leftarrow$  select a random cut of  $P$ 
6      $\epsilon_a \leftarrow |A(P_1) - w_1 \cdot A(P)|$  // Area prop. error
7      $\epsilon_c \leftarrow 1 - \frac{R(P_1)+R(P_2)}{2}$  // Circularity error
8      $error \leftarrow \alpha \cdot \epsilon_a + (1 - \alpha) \cdot \epsilon_c$ 
9     if  $error < best\_error$  then
10       $best\_cut, best\_error \leftarrow (P_1, P_2), error$ 
11  return  $best\_cut$ 

```

Algorithm 4: Partitioning a polygon into k sub-polygons

Input: A list of sibling nodes $[T_1, \dots, T_k]$ and a polygon P
Output: k sub-polygons, each relative to a sibling

```

1 Procedure PARTITION( $[T_1, \dots, T_k]$ ):
2    $partitions \leftarrow []$ ;  $P_r \leftarrow P$  //  $P_r$  starts as the whole  $P$ 
3   for  $T_i \in [T_1, \dots, T_k]$  do
4     if  $i = n$  then
5       Append  $P_r$  to  $partitions$  // Final polygon
6     else
7        $weight \leftarrow \frac{F(T_i)}{\sum_{j=i}^k F(T_j)}$  // Area fraction of  $T_i$ 
8        $P_i, P_r \leftarrow$  POLYGON_CUT( $P_r, weight$ )
9       Append  $P_i$  to  $partitions$ 
10  return  $partitions$ 

```

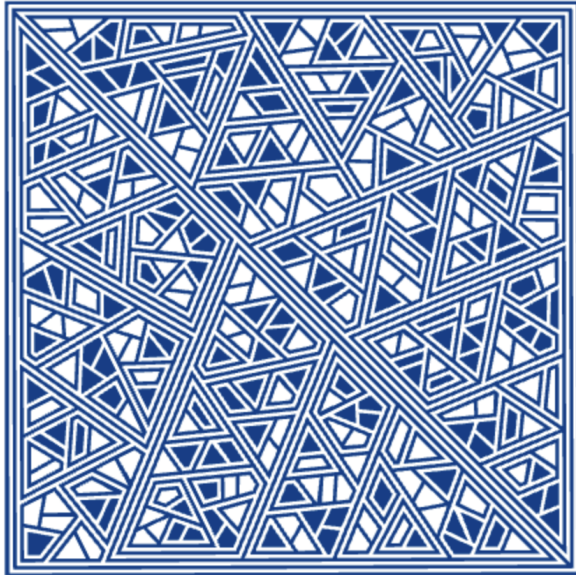


Fig. 10. "This Claycode packs more than 500 nodes ✨"

As with ϕ , the constant α can be tuned to achieve different aesthetics, but in our implementation we fixed it to 0.6, thus biasing the optimization towards a better area proportionality. Instead of directly searching for a solution of eq. (6), we first solve the binary instance of the problem (*i.e.*, involving only two siblings), and then lift the solution to the general case. A simplified formula for the binary case (derived in appendix B) is given by:

$$\min_{[P_1, P_2] \in \mathcal{P}} \alpha |A(P_1) - w_1 A(P)| + (1 - \alpha) \left(1 - \frac{R(P_1) + R(P_2)}{2} \right) \quad (7)$$

where w_1 is the fraction of the total area that we intend P_1 to occupy, *i.e.*, $\frac{F(T_1)}{F(T_1)+F(T_2)}$. A solution to eq. (7) is found using a straightforward random search (algorithm 3). In our solution, we prune the search space by only considering partitions that can be obtained through straight-line cuts. A *cut* of a polygon P is a binary partition of P formed by a segment whose endpoints lie on the perimeter of P . In our implementation, we upper-bounded the search to 400 solutions, and stopped early in case of convergence.

Using algorithm 3 as a building block, we define the PARTITION procedure in algorithm 4. Each iteration of the algorithm processes a single sibling T_i , weighting its footprint against the combined footprint of all its rightmost siblings T_{i+1}, \dots, T_k . The subsequent invocation of algorithm 3 produces two new polygons: P_i , which is assigned to T_i , and P_r , dedicated to all the rightmost siblings of T_i . Repeating this process $k - 1$ times results in a full partition.

5 Scanner

To complete the Claycode's pipeline we discuss the *scanner*, a module that performs the inverse of the encoding pipeline (fig. 2), retrieving the original message from a visual representation of a Claycode.

This module is designed to run on a smartphone, using the camera to frame the code and extract the information contained. Unlike most 2D codes, Claycodes do not have a predefined shape or visual anchor, such as the finding patterns of QR codes [Tiwari 2016]. The Claycode's scanner cannot hence rely on the classic paradigm of first isolating the subset of the input image containing the code and then focusing on its pixels for decoding. Our method, illustrated in fig. 11, begins instead by transforming the input image into a *global topology tree*, without explicitly searching for a Claycode. We call this phase *global topology extraction*. The underlying assumption is that, if a Claycode is framed within the input image, then its topology must be a subtree of the global topology tree. Once the global topology tree is extracted, the input image is discarded, and the scanner analyses the topology to extract all the contained messages. We call this phase *Claycode identification*.

5.1 Global Topology Extraction

The procedure begins with a camera frame, which is filtered and then processed to build its topological structure. The process is designed to prepare an image for contour detection by enhancing important features while reducing irrelevant details.

Let $I_{\text{RGB}}(x, y)$ be the input RGB image, with x, y as their pixel coordinates. First, the image is converted to grayscale $I_{\text{gray}}(x, y)$, simplifying the input to intensity variations. Then, to remove noise

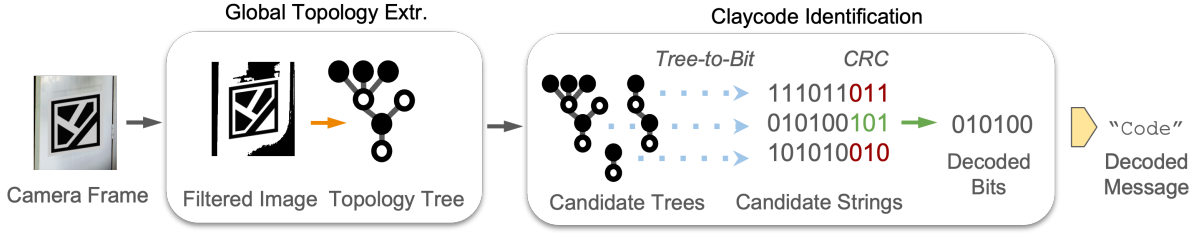


Fig. 11. The pipeline followed by the scanner.

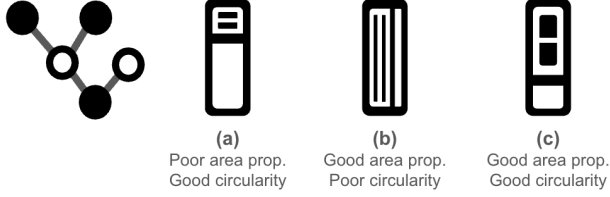


Fig. 12. Three instances of packing. The topology on the left is fit in a tall and narrow rectangle, showing the importance of both circularity and area distribution to maximize the readability of the code.

while preserving edges, a bilateral filter [Kornprobst et al. 2009] is applied, producing $I_{bil}(x, y)$, which smooths the image while retaining boundary details. The filtered image is then binarized through adaptive thresholding:

$$B(x, y) = \begin{cases} 1, & \text{if } I_{bil}(x, y) > \tau(x, y), \\ 0, & \text{otherwise.} \end{cases} \quad (8)$$

Here $\tau(x, y) = \frac{1}{n} \sum_{(i,j) \in N(x,y)} I_{bil}(i, j) - K$ is the local threshold value calculated for the pixel (x, y) based on the intensity values in its neighborhood $N(x, y)$. The size of $N(x, y)$ is defined by the block size, which is typically a small odd integer depending on the size of the input image; n is the square block size and K is a constant subtracted from the mean to fine-tune the threshold. $B(x, y)$ serves as an input for the Suzuki-Abe algorithm [Bradski 2000; Suzuki and Abe 1985] for contour extraction, where the boundaries of connected regions are identified and organized into a hierarchy (algorithm is detailed in appendix C), resulting in the global topology tree of the image T_f . Note that the thresholding operation does not prevent the use of colors (figs. 10, 15 and 18), but neighboring regions must be sufficiently contrasted, in order to ensure that the boundary is detected.

5.2 Claycode Identification

From this point forward, the scanner exclusively operates on T_f , identifying and decoding all Claycodes in the scene. On our test smartphone, $|D(T_f)|$ typically contains thousands of nodes. While some may represent the root of a Claycode, most are noise. To accelerate processing, we first construct a subset of candidate roots using a simple heuristic:

$$\mathbf{T} = \{T \in D(T_f) : |D(T)| > n\}, \quad (9)$$

In our implementation, $n = 10$. The heuristic guarantees that no valid Claycode is discarded – no Claycode is so simple as to contain only ten nodes – and averagely prunes more than 99% of the nodes, since real-world topologies are predominantly flat (fig. 14).

Each identified potential Claycode $T \in \mathbf{T}$ is then transformed into a bit string using the function $g(T)$ described in section 3:

$$\mathbf{B} = \{g(T) \mid T \in \mathbf{T}\}. \quad (10)$$

At this point, we obtain a set of potential message candidates, containing a mixture of messages (one for each Claycode in the scene) and noise. To filter the valid messages, we designed the encoding pipeline to append a 16-bit Cyclic Redundancy Code (CRC), denoted as b_{CRC} , to each message b_{msg} . In our implementation, we adopted the same polynomial of the CRC-15/CAN protocol *i.e.*, 0x4599 [Bosch GmbH 1991]. As a final step, all candidate bit strings $b \in \mathbf{B}$ are validated using the CRC, resulting in the final list of decoded Claycode payloads:

$$\mathbf{B}^* = \{b_{msg} \mid b = b_{msg} : b_{CRC}, b \in \mathbf{B}, \text{CRC}(b_{msg}) = b_{CRC}\} \quad (11)$$

We found the CRC to be extremely effective avoiding false positives, especially in the case of damaged Claycodes. In section 6 we have used our implementation to scan thousands of Claycodes without experiencing a single false positive. This is a significant achievement, as false positives are a key challenge in topological codes, as exemplified by SeedMarkers [Getschmann and Ehtler 2021] and D-Touch [Costanza and Robinson 2003].

Redundancy scheme. The CRC functions solely as an error detection mechanism and does not enable the recovery of partially corrupted messages. Traditional error correction schemes, such as [Reed and Solomon 1960], are not viable: a single error in the topology tree usually propagates through the tree-to-bit function into several bit flips and often even alters the length of the message. To provide some resistance to occlusion damage, we implement a simple redundancy scheme based on the fact that Claycode’s scanner natively processes multiple candidate messages simultaneously. We modify the bit-tree encoding function of section 3 to generate a new tree T_R such that $C(T_R) = [f(b), f(b)]$. The approach can be extended to any number of copies, and critically improves the resistance of the codes, at the price of the code’s data capacity. We refer to the number of copies in the Claycode as *redundancy level* R , normally set to 1 (*i.e.*, only one copy of $f(b)$ is present).

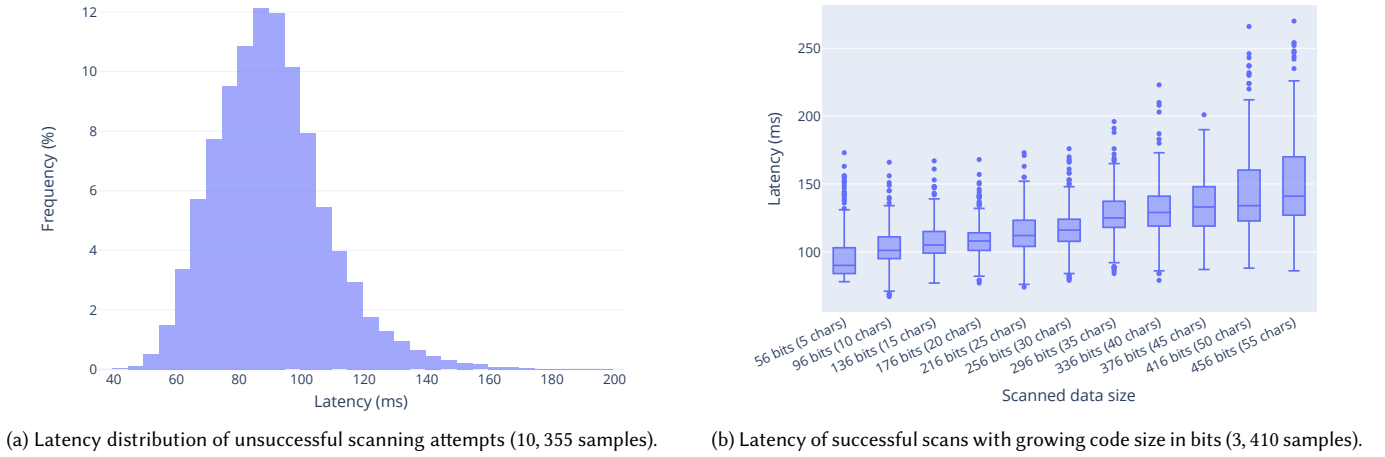


Fig. 13. Scanner pipeline end-to-end latency analysis.

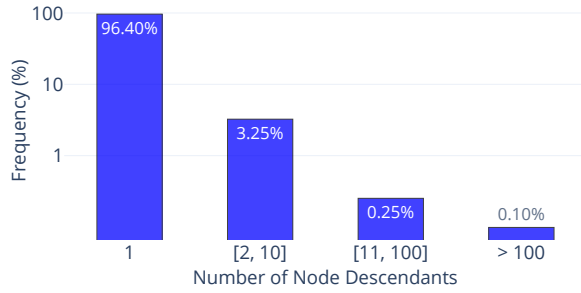


Fig. 14. Number of descendants for each node in 1,039 global topology trees (six million nodes) derived from real-world images.



Fig. 15. "Pizza!"

5.3 Scanning Latency

To assess the performance of the scanner application, we measured the end-to-end latency for each scan attempt on our test device,

a Google Pixel 8 Pro (12GB RAM, running Android 15). Images were captured using the primary back camera at a resolution of 1920×1920 . Although there is no hard upper limit on the duration of the scanning pipeline, we established a target average latency of 100ms under typical conditions. This target allows for 10 scanning attempts per second on average, which aligns with the performance of existing scanning technologies [Yang et al. 2018].

We fixed the phone to a tripod and ran the scanner for eight minutes while it was pointed at a screen. The displayed footage featured scenes of varying complexity—such as portrait close-ups, landscapes, and abstract patterns—to fully exercise the pipeline. To incorporate real-world footage, we also handheld the phone and recorded for another eight minutes while walking indoors and outdoors. Notably, no Claycode was scanned during this experiment. As shown in fig. 13a, we achieved an average latency of 90.2ms, with a standard deviation of 18ms and 10, 335 samples in the dataset. The minimum and maximum latency are 42ms and 196ms, respectively.

Experiment 2 – Latency of successful scans. The phone was fixed in place and pointed at a screen displaying black-and-white Claycodes, each encoding a randomly-generated alphanumeric message. We varied the encoded data sizes from 56 to 456 bits, with a step size of 40 bits (5 characters). For each data size, we generated 310 Claycodes with random alphanumeric content, resulting in a total of 3, 410 samples. Each code was displayed for 5 seconds. As illustrated in fig. 13b, the average scan latency increased approximately linearly with code size, ranging from 97ms (for 56 bits) to 148ms (for 456 bits), with observed extremes between 67ms and 270ms. When compared to fig. 13a, it is evident that latency is affected by the additional processing involved in detecting and decoding Claycodes. Nevertheless, this latency corresponds only to the final iteration of the scanning loop—which runs approximately 10 times per second—and thus has a limited impact on the overall performance.

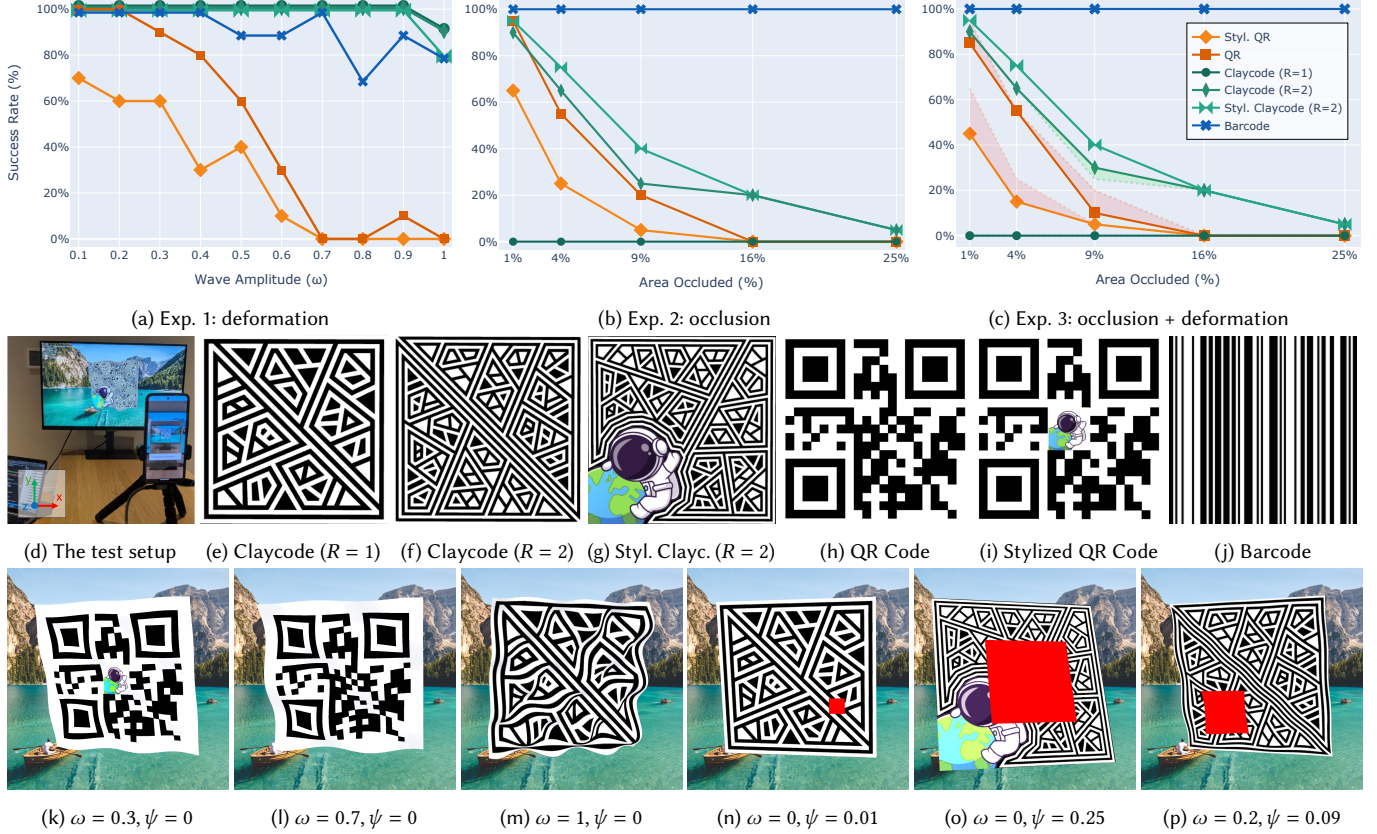


Fig. 16. The comparative evaluation between Claycodes, QR Codes, and Code128-Barcodes presented in section 6.

6 Comparative Evaluation

Scannable codes, whether printed or displayed on screens, are often subject to environmental wear and adverse scan conditions, such as the quality of camera hardware, lens distortion, uneven surfaces and scanning angle. To assess Claycode's robustness, we conducted an empirical study to measure its performance in a controlled environment compared to other popular 2D scannable codes.

6.1 Experiment Setup

We compared $K = 6$ different types of codes: Claycodes (redundancy level $R = 1$), Claycodes ($R = 2$), stylized Claycodes ($R = 2$), QR Codes (*high* error correction level), stylized QR Codes (*high* error correction level) and Code128-Barcodes. Barcodes are 1D codes and are included as a baseline. We generated $M = 10$ alphanumeric random strings and produced a code for each code type, resulting in $K \cdot M = 60$ different codes. To ensure reproducibility in a controlled environment, while performing the evaluation on representative hardware, we fixed an Android phone (Google Pixel 8 Pro, as described in section 5.3) on a tripod, at a fixed distance from a 24-inch screen, as shown in fig. 16d. The codes were rendered one by one in a 3D environment in the form of a textured plane mesh, modified to simulate different kinds of tampering and scanning conditions. We varied a diverse set of parameters. First, the **scanning angles** $\phi_x, \phi_y \in [-20^\circ, -10^\circ] \cup [+10^\circ, +20^\circ]$ were simulated by rotating the

mesh on the x and y axes. We never set the scanning angle to zero, as it is rarely the case in real-world scans. The **deformation damage** was simulated by introducing a wave-like oscillation in the plane mesh, in the form of an offset to the z (depth) component of the mesh, in such a way that $z(x, y) = \omega \cdot \sin(v_x \cdot x) \cdot \cos(v_y \cdot y)$, where the frequencies $(v_x, v_y) \in [1, 2]$ were picked at random, while the wave amplitude $\omega \in [0, 1]$ was adopted as the measure of deformation. To simulate **occlusion damage**, we overlaid a red square on the mesh texture, as shown in figs. 16n, 16o and 16p. The square's size, defined as a percentage of the total area $\psi \in [0, 1]$, was adopted as a measure of occlusion, while its location (ρ_x, ρ_y) was randomly selected ensuring the entirety of the square overlaps the texture. We call each combination of parameters $(\phi_x, \phi_y, \omega, v_x, v_y, \psi, \rho_x, \rho_y)$ a *scenario*. In each experiment, we generated a set of scenarios and then evaluated them against the dataset of $K \cdot M$ codes. Each test case was considered either a success (the code was scanned) or a failure (the code was not scanned, or it was incorrectly scanned – which has only happened with barcodes). Before considering a test case failed, we allowed some seconds for the scanner to recognize the code, and played an animation that adjusted the mesh size by smoothly increasing it to 1.3 times its original size, then reducing it to 0.7 times its size, and finally returning it to its initial dimensions. We decided to do so as varying the zoom is compatible with most real-life scenarios, and because we found barcodes to be particularly

sensitive to zooming conditions. We scanned Claycodes using an Android implementation of the scanner described in section 5, while for QR Codes and barcodes we used the commercially-available app developed by [Gamma Play 2024], which to-date is top-rated and counts hundreds of millions of downloads.

6.2 Results

We performed three experiments, first considering deformations and occlusions as mutually exclusive features (experiments 1 and 2), and finally combining them in the last batch of our experiment.

Experiment 1 – deformations. In our first experiment, we studied the impact of deformations on scannability, in the absence of occlusion. For each of the $K \cdot M = 60$ codes, we randomly generated 10 different scenarios by varying ω from 0.1 to 1 with a step size of 0.1, for a total of 600 scans. We fixed $\psi = 0$ (codes were never occluded), and randomly sampled the remaining parameters. As shown in fig. 16a, Claycodes succeeded in nearly all cases until $\omega = 1$ (fig. 16m), where they started to show some minimal degradation. Comparatively, QR Code’s performance started dropping at $\omega = 0.3$ (fig. 16k), and failed in almost all scenarios with $\omega \geq 0.7$ (fig. 16l). Stylized QR Codes performed the worst, starting with a 70% success rate for $\omega = 0.1$, and converging to zero for $\omega \geq 0.7$.

Experiment 2 – occlusions. In this experiment, we focused on occlusion damage in the absence of deformation. For each of the $K \cdot M = 60$ codes, we randomly generated 10 different scenarios by varying ψ across the set $\{0.01, 0.04, 0.09, 0.16, 0.25\}$, with two samples for each value of ψ , and a total of 600 scans. We fixed $\omega = 0$ to eliminate any deformation, and all other parameters were randomly sampled. As shown in fig. 16b, Claycodes with redundancy level $R = 1$ do not tolerate any kind of occlusion (fig. 16n), but almost always perform better than QR codes for $R = 2$. Interestingly, stylized Claycodes outperform non-stylized ones. This is because the overlaid square sometimes partially or completely occludes the art, as opposed to the payload – the same is true for QR codes.

Experiment 3 – deformations and occlusions. Finally, we repeated experiment 2 on the same dataset of scenarios, but fixed to $\omega = 0.2$. We chose this value (an example is provided in fig. 16p) because $\omega = 0.2$ had no effect on the scannability of non-stylized QR Codes (fig. 16b). As shown in fig. 16c, the impact of the added deformation is not present in Claycodes. Conversely, the added deformation further reduces the success rate of QR Codes, showing how the deformation and occlusion damage compounds.

7 Evaluation Across Physical Media and Lighting Scenarios

To further understand the practical limitations of Claycodes in real-world scenarios, we conducted a second evaluation that considered variations in physical media and environmental lighting. We printed a set of 4 QR Codes and 8 Claycodes with varying designs, sizes, and colors, on both matte and glossy paper, and tested them across 7 distinct physical scenarios, each featuring different backgrounds and lighting conditions. In contrast to the controlled setup in section 6, this evaluation recreated a natural user experience: a

person attempted to scan each code as they normally would. Each scanning attempt was classified as a success (✓) if the code was scanned in under three seconds without requiring any adjustment of the phone; a partial success (✦) if scanning required repositioning or readjustment; or a failure (✗) if the code could not be scanned within ten seconds. We scanned each code twice, and assigned the final outcome based on the lower-performing attempt: two successes were recorded as a success, a combination of success and partial success was recorded as a partial success, and any attempt that included a failure was recorded as a failure. The physical scenarios used in this evaluation are shown in fig. 17:

- **Outside** (fig. 17a). A balcony in direct sunlight.
- **Inside** (fig. 17b). A well-lit room with diffuse natural light.
- **Low, uneven light** (fig. 17d). A partially illuminated room. Noticeable lighting variations on the surface of the code.
- **Dark** (fig. 17e). A room with low uniform illumination.
- **Strong reflections** (fig. 17f). A circular LED lamp is directed at the code, creating a harsh glare. The user must scan the code through the central opening of the lamp.
- **Carafe, inwards** (fig. 17h). The code is bent inward and placed inside a transparent carafe, introducing surface distortion, visual noise, and partial occlusion.
- **Carafe, outwards** (fig. 17i). As above, but with the code bent outward along the curvature of the carafe.

As can be seen in table 1, all codes performed reliably under *natural light*—both outdoors and indoors—as well as in *low, uneven lighting* conditions. The few partial successes observed for Claycodes in these three scenarios were related to camera focus issues, which we consider orthogonal to the method itself and reflective of implementation limitations.

In the *dark* scenario, several Claycodes failed to scan successfully. As expected, designs with less contrasted colors generally performed worse. However, Claycodes with greater redundancy (*i.e.*, higher R) were particularly prone to failure in this condition: while redundancy can recover a partially occluded code, it also increases its visual complexity, making it more difficult to decode in low-light environments.

In the *strong reflections* scenario, the difference between matte and glossy paper became more pronounced. Codes with higher redundancy generally performed better: as illustrated in fig. 17g, glare acts similarly to the occlusion damage modeled in section 6, and redundancy helped mitigate its effect.

The carafe experiments (figs. 17h and 17i) proved to be the most challenging overall for both QR Codes and Claycodes, due to a combination of distortion, partial occlusions, noise introduced by the semitransparent glass, and shadows. QR Codes were primarily hindered by distortion but would typically scan successfully once the user adjusted their position to minimize the perceived curvature. In contrast, Claycodes exhibited poorer performance with low-contrast codes but were generally scannable from multiple viewing angles.

Overall, the evaluation indicates that Claycodes are generally robust and versatile, although several areas for practical improvement remain, largely tied to the scanner’s image preprocessing implementation: enhancements such as improved autofocus, adaptive zoom, and an ensemble of image pre-processing pipelines is likely to improve decoding performance in adverse conditions.

Table 1. Experiment Evaluation Results

		Screen (baseline)	Outside (nat. light)		Inside (nat. light)		Low uneven light		Dark		Strong reflections		Carafe (Inwards)		Carafe (Outwards)	
			Matte	Glossy	Matte	Glossy	Matte	Glossy	Matte	Glossy	Matte	Glossy	Matte	Glossy	Matte	Glossy
QRCode	"baseline"	✓	✓	✓	✓	✓	✓	✓	✓	✓	✓	✓	✗	✗	✗	✗
	"Scan Me"	✓	✓	✓	✓	✓	✓	✓	✓	✓	✓	✓	✗	✗	✗	✗
	"colors!" (coloured)	✓	✓	✓	✓	✓	✓	✓	✓	✓	✓	✓	✗	✗	✗	✗
	"eye" (stylised)	✓	✓	✓	✓	✓	✓	✓	✗	✗	✗	✗	✗	✗	✗	✗
Claycode	"claycode" (R = 1)	✓	✓	✓	✓	✓	✓	✓	✓	✓	✗	✗	✓	✓	✓	✗
	"👁️" (R = 1)	✓	✓	✓	✓	✓	✓	✓	✓	✓	✗	✗	✓	✓	✓	✓
	"space" (R = 1)	✓	✓	✓	✓	✓	✓	✓	✓	✓	✗	✗	✗	✗	✓	✓
	"pizza!" (R = 1)	✓	✓	✓	✗	✗	✓	✓	✓	✓	✗	✗	✗	✗	✓	✓
	"magic" (R = 1)	✓	✓	✓	✓	✓	✓	✗	✗	✗	✗	✗	✗	✗	✗	✗
	"claycode.io" (R = 2)	✓	✓	✓	✓	✓	✓	✗	✗	✗	✗	✗	✓	✗	✗	✗
	"SIGGRAPH!" (R = 2)	✓	✗	✗	✗	✗	✓	✓	✗	✗	✓	✓	✗	✗	✗	✗
	"Giraffe!" (R = 7)	✓	✓	✓	✓	✓	✗	✗	✗	✗	✗	✗	✗	✗	✓	✗

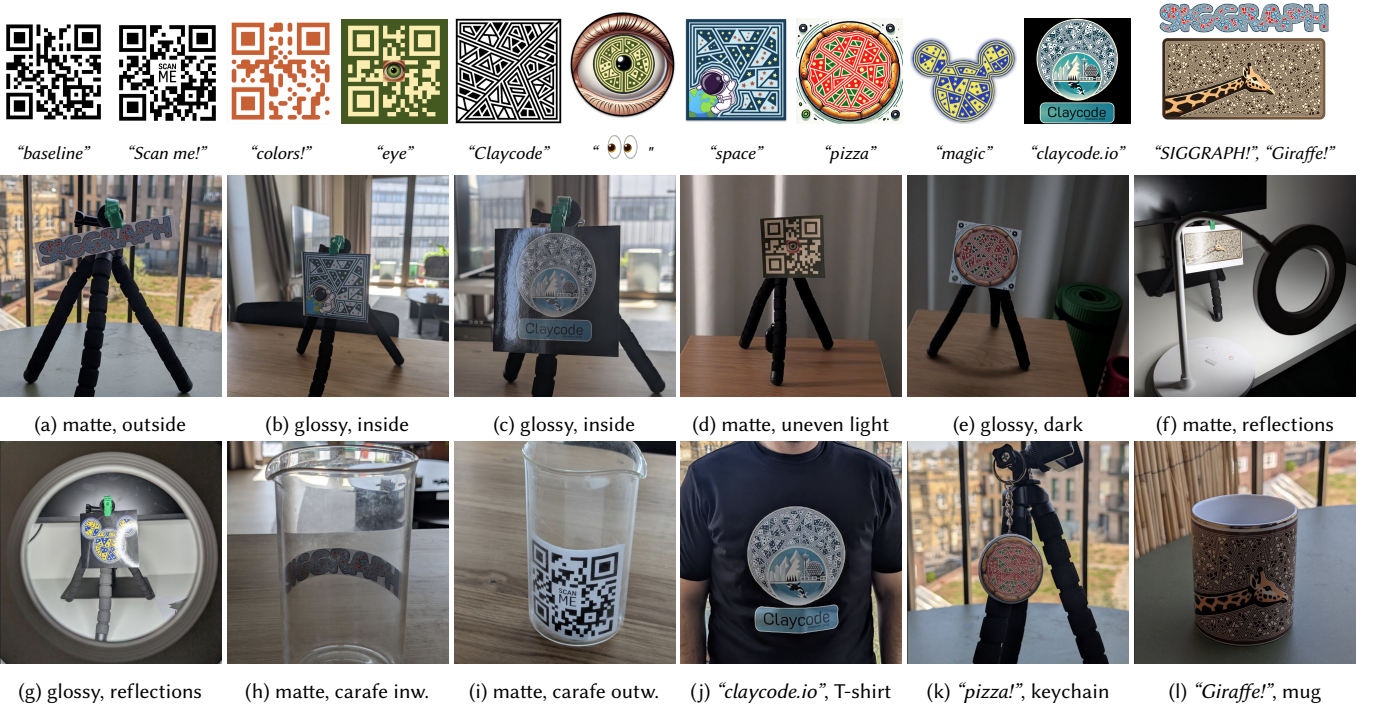


Fig. 17. The evaluation on printed media presented in section 7.



Fig. 18. "SIGGRAPH"

7.1 Discussion on Additional Media

To further examine the versatility of Claycodes as design artifacts, we applied a selection of designs to various physical media: a cotton T-shirt (fig. 17j), a ceramic mug (fig. 17l), and a metallic keychain (fig. 17k). We replicated the evaluation protocol described in table 1, excluding the *carafe* condition, and observed broadly consistent outcomes. All three objects were successfully scanned under natural lighting conditions, exhibited reduced performance under *low*, *uneven light*, and failed to decode in the *dark* scenario. The highly reflective metallic keychain proved particularly susceptible to scanning failure in the *strong reflections* setting, while the T-shirt performed notably well. Textiles appear to be a promising medium for printed Claycodes, as the scanner is generally unaffected by natural wrinkles and creases. In the case of the T-shirt, no manual straightening was ever required to scan the code.

8 Conclusion

In this paper, we introduced Claycode, a novel type of 2D scannable code based on topological encoding. We have detailed the encoding/decoding pipeline and demonstrated that Claycodes are highly stylable and extremely tolerant to deformations. In all experiments, stylized Claycodes consistently performed equally or better than their non-stylized counterparts, showing that incorporating artistic elements does not negatively impact reliability. This stands in contrast with QR codes, where adding artistic features comes at the cost of damaging the code.

In the future, we intend to improve the data capacity of Claycodes by abandoning UTF-8, in favor of a multimodal character encoding, devising more space-efficient bit-tree encodings, and implementing error correction schemes that go beyond the redundancy of the topology. Additionally, we plan to improve the reliability of the scan under challenging conditions, such as blur and poor lighting, by leveraging neural techniques similar to those applied to QR codes by [Chou et al. 2015]. In Claycodes, these techniques could further enable topology inference under partial occlusion, improving the robustness of Claycodes with no redundancy ($R = 1$).

Acknowledgments

We thank Kimaya Bedarkar, Stratis Tsirtsis, and Valerio Di Donato for their valuable suggestions and discussions.

References

- Y Abe. 1994. Tree representation of positive integers. *Applied Mathematics Letters* 7, 1 (1994), 57.
- Apple. 2020. Human Interface Guidelines: App Clips. <https://developer.apple.com/design/human-interface-guidelines/app-clips/>. Accessed: 2024-12-30.
- Ross Bencina and Martin Kaltenbrunner. 2005. Improved Topological Fiducial Tracking in the reacTIVision System. In *2005 IEEE Computer Society Conference on Computer Vision and Pattern Recognition (CVPR'05) - Workshops*. 99–99. <https://doi.org/10.1109/CVPR.2005.475>
- Terry Beyer and Sandra Mitchell Hedetniemi. 1980. Constant time generation of rooted trees. *SIAM J. Comput.* 9, 4 (1980), 706–712.
- Bosch GmbH. 1991. *CAN Specification Version 2.0*. Technical Report. Robert Bosch GmbH, Stuttgart, Germany. <https://www.bosch-semiconductors.com/can> Available from Bosch Automotive Electronics.
- Gary Bradski. 2000. The OpenCV Library. *Dr. Dobbs's Journal of Software Tools* (2000).
- Peter Cappello. 1988. A new bijection between natural numbers and rooted trees. In *4th SIAM Conference on Discrete Mathematics*. Citeseer.
- Changsheng Chen, Wenjian Huang, Baojian Zhou, Chenchen Liu, and Wai Ho Mow. 2016. PiCode: A New Picture-Embedding 2D Barcode. *IEEE Transactions on Image Processing* 25, 8 (2016), 3444–3458. <https://doi.org/10.1109/TIP.2016.2573592>
- Xiaorui Chen and Sara McMains. 2005. Polygon offsetting by computing winding numbers. In *International Design Engineering Technical Conferences and Computers and Information in Engineering Conference*, Vol. 4739. 565–575.
- Tzu-Han Chou, Chuan-Sheng Ho, and Yan-Fu Kuo. 2015. QR code detection using convolutional neural networks. In *2015 International Conference on Advanced Robotics and Intelligent Systems (ARIS)*. 1–5. <https://doi.org/10.1109/ARIS.2015.7158354>
- Hung-Kuo Chu, Chia-Sheng Chang, Ruen-Rone Lee, and Niloy J Mitra. 2013. HalfTone QR codes. *ACM Transactions on Graphics (TOG)* 32, 6 (2013), 1–8.
- Enrico Costanza and Jeffrey Huang. 2009. Designable visual markers. *Conference on Human Factors in Computing Systems - Proceedings* (04 2009). <https://doi.org/10.1145/1518701.1518990>
- Enrico Costanza and John Robinson. 2003. A Region Adjacency Tree Approach to the Detection and Design of Fiducials. (2003).
- Enrico Costanza, Simon Shelley, and John Robinson. 2003. D-touch: A Consumer-Grade Tangible Interface Module and Musical Applications. (01 2003).
- EP Cox. 1927. A method of assigning numerical and percentage values to the degree of roundness of sand grains. *Journal of paleontology* 1, 3 (1927), 179–183.
- Russ Cox. 2012. Qartcodes. <http://research.swth.com/qart>. Accessed: 2025-01-02.
- Universidad de Alicante. Patent ES2616146A1, 2016. Method of detection and recognition of visual markers of long reach and high density.
- Mustafa Doga Dogan, Vivian Hsinyueh Chan, Richard Qi, Grace Tang, Thijs Roumen, and Stefanie Mueller. 2023a. StructCode: Leveraging Fabrication Artifacts to Store Data in Laser-Cut Objects. In *Proceedings of the 8th ACM Symposium on Computational Fabrication (SCF '23)*. Association for Computing Machinery, 1–13. <https://doi.org/10.1145/3623263.3623353>
- Mustafa Doga Dogan, Raul Garcia-Martin, Patrick William Haertel, Jamison John O'Keefe, Ahmad Taka, Akarsh Aurora, Raul Sanchez-Reillo, and Stefanie Mueller. 2023b. BrightMarker: 3D Printed Fluorescent Markers for Object Tracking. In *Proceedings of the 36th Annual ACM Symposium on User Interface Software and Technology (UIST '23)*. Association for Computing Machinery, 1–13. <https://doi.org/10.1145/3586183.3606758>
- Mustafa Doga Dogan, Ahmad Taka, Michael Lu, Yunyi Zhu, Akshat Kumar, Aakar Gupta, and Stefanie Mueller. 2022. InfraredTags: Embedding Invisible AR Markers and Barcodes Using Low-Cost, Infrared-Based 3D Printing and Imaging Tools. In *Proceedings of the CHI Conference on Human Factors in Computing Systems (CHI)*. Association for Computing Machinery, 1–12. <https://doi.org/10.1145/3491102.3501951>
- Brice Effantin. 2004. Generation of Unordered Binary Trees. In *Computational Science and Its Applications—ICCSA 2004: International Conference, Assisi, Italy, May 14–17, 2004, Proceedings, Part III* 4. Springer, 648–655.
- Martin Feick, Xuxin Tang, Raul Garcia-Martin, Alexandru Luchianov, Roderick Wei Xiao Huang, Chang Xiao, Alexa Siu, and Mustafa Doga Dogan. 2025. Imprinto: Enhancing Infrared Inkjet Watermarking for Human and Machine Perception. In *Proceedings of the CHI Conference on Human Factors in Computing Systems (CHI)*. Association for Computing Machinery, to appear. <https://doi.org/10.1145/3491102.3501951>
- Mark Fiala. 2004. ARTag Revision 1, A Fiducial Marker System Using Digital Techniques. (01 2004).
- Flowcode. 2024. Flowcode: Create and Share QR Codes Instantly. <https://www.flowcode.com/>. Accessed: 2024-12-30.
- Gamma Play. 2024. QR Code Scanner. https://play.google.com/store/apps/details?id=com.gamma.scan&hl=en_GB. Accessed: 2025-01-20.
- Christopher Getschmann and Florian Ehtler. 2021. Seedmarkers: Embeddable Markers for Physical Objects. 1–11. <https://doi.org/10.1145/3430524.3440645>
- Shinichi Higashino, Sakiko Nishi, and Ryuuki Sakamoto. 2016. ARTTag: aesthetic fiducial markers based on circle pairs. In *ACM SIGGRAPH 2016 Posters*. 1–2.
- ISO. 2007. ISO/IEC 15417:2007 Information technology – Automatic identification and data capture techniques – Bar code symbology specification – Code 128. <https://www.iso.org/standard/43896.html>
- Joshua D. A. Jung, Rahul N. Iyer, and Daniel Vogel. 2019. Automating the Intentional Encoding of Human-Designable Markers. In *Proceedings of the 2019 CHI Conference on Human Factors in Computing Systems (CHI)*. Association for Computing Machinery, 187:1–187:12. <https://doi.org/10.1145/3290605.3300417>
- Joshua D. A. Jung and Daniel Vogel. 2018. Methods for Intentional Encoding of High Capacity Human-Designable Visual Markers. In *Proceedings of the 2018 CHI Conference on Human Factors in Computing Systems (CHI '18)*. Association for Computing Machinery, 313:1–313:12. <https://doi.org/10.1145/3173574.3173887>
- Pierre Kornprobst, Jack Tumblin, and Frédo Durand. 2009. Bilateral Filtering: Theory and Applications. *Foundations and Trends in Computer Graphics and Vision* 4 (01 2009), 1–74. <https://doi.org/10.1561/06000000020>
- Wendy Kurniawan, Hiroshi Okumura, Muladi Muladi, and Anik Handayani. 2019. An Improvement on QR Code Limit Angle Detection using Convolution Neural Network. In *International Conference on Electrical, Electronics and Information Engineering (ICEEIE)*. 234–238. <https://doi.org/10.1109/ICEEIE47180.2019.8981449>
- Dingzeyu Li, Avinash S. Nair, Shree K. Nayar, and Changxi Zheng. 2017. AirCode: Unobtrusive Physical Tags for Digital Fabrication. In *Proceedings of the 30th Annual ACM Symposium on User Interface Software and Technology (UIST)*. Association for Computing Machinery, 449–460. <https://doi.org/10.1145/3126594.3126641>

- Gang Li. 1997. *Generation of rooted trees and free trees*. University of Victoria.
- Shih-Syun Lin, Min-Chun Hu, Chien-Han Lee, and Tong-Yee Lee. 2015. Efficient QR Code Beautification With High Quality Visual Content. *IEEE Transactions on Multimedia* 17, 9 (2015), 1515–1524. <https://doi.org/10.1109/TMM.2015.2437711>
- Yu-Hsun Lin, Yu-Pei Chang, and Ja-Ling Wu. 2013. Appearance-based QR code beautifier. *IEEE Transactions on Multimedia* 15, 8 (2013), 2198–2207.
- Henrique Teles Maia, Dingzeyu Li, Yuan Yang, and Changxi Zheng. 2019. LayerCode: Optical Barcodes for 3D Printed Shapes. *ACM Transactions on Graphics (TOG)* 38, 4 (2019), 90:1–90:13. <https://doi.org/10.1145/3306346.3322960>
- J. Mark Keil. 2000. Chapter 11 - Polygon Decomposition. In *Handbook of Computational Geometry*, J.-R. Sack and Jorge Urrutia (Eds.). North-Holland, Amsterdam, 491–518. <https://doi.org/10.1016/B978-044482537-7/50012-7>
- Elif Ozkaya, H Erkan Ozkaya, Juanita Roxas, Frank Bryant, and Debbora Whitson. 2015. Factors affecting consumer usage of QR codes. *Journal of Direct, Data and Digital Marketing Practice* 16 (2015), 209–224.
- Paul Pollack and Enrique Treviño. 2018. Finding the Four Squares in Lagrange's Theorem. *Integers* 18, A15 (2018), 7–17.
- QRCode AI. 2024. QRCode AI: Advanced QR Code Generator. <https://qrcode-ai.com/>. Accessed: 2024-12-30.
- Irving S Reed and Gustave Solomon. 1960. Polynomial codes over certain finite fields. *Journal of the society for industrial and applied mathematics* 8, 2 (1960), 300–304.
- Takeaki Uno Shin-ichi Nakano. 2003. Efficient generation of rooted trees. (2003).
- Osvaldo Skliar, Sherry Gapper, and Ricardo E. Monge Monge. 2020. A One-to-One Correspondence between Natural Numbers and Binary Trees. *arXiv preprint arXiv:2002.04477* (2020).
- Spotify. 2017. Spotify Codes - Share music the easy way. <https://www.spotifycodes.com/>. Accessed: 2024-12-30.
- Hao Su, Jianwei Niu, Xuefeng Liu, Qingfeng Li, Ji Wan, Mingliang Xu, and Tao Ren. 2021. Artcoder: an end-to-end method for generating scanning-robust stylized qr codes. In *Proceedings of the IEEE/CVF Conference on Computer Vision and Pattern Recognition*. 2277–2286.
- Satoshi Suzuki and Keiichi Abe. 1985. Topological structural analysis of digitized binary images by border following. *Comput. Vis. Graph. Image Process.* 30 (1985), 32–46. <https://api.semanticscholar.org/CorpusID:205113350>
- Matthew Tancik, Ben Mildenhall, and Ren Ng. 2020. StegaStamp: Invisible Hyperlinks in Physical Photographs. In *Proceedings of the IEEE/CVF Conference on Computer Vision and Pattern Recognition (CVPR)*. IEEE, 2117–2126. <https://doi.org/10.1109/CVPR42600.2020.00219>
- Sumit Tiwari. 2016. An introduction to QR code technology. In *2016 international conference on information technology (ICIT)*. IEEE, 39–44.
- Nan Wan, Pengcheng Zhang, Zuheng Liu, Zhe Li, Wei Niu, Xiuye Rui, Shibo Wang, Myeongsu Seong, Pengbo He, Siqi Liang, et al. 2023. Implantable QR code subcutaneous microchip using photoacoustic and ultrasound microscopy for secure and convenient individual identification and authentication. *Photoacoustics* 31 (2023), 100504.
- Chang Xiao, Cheng Zhang, and Changxi Zheng. 2018. FontCode: Embedding Information in Text Documents Using Glyph Perturbation. *ACM Transactions on Graphics (TOG)* 37, 2 (2018), 15:1–15:16. <https://doi.org/10.1145/3152823>
- Yuqiu Xie, Bolin Jiang, Jiawei Li, Naiqi Li, Bin Chen, Tao Dai, Yuang Peng, and Shu-Tao Xia. 2024. GladCoder: Stylized QR Code Generation with Grayscale-Aware Denoising Process. In *International Joint Conference on Artificial Intelligence*. <https://api.semanticscholar.org/CorpusID:271504025>
- Mingliang Xu, Qingfeng Li, Jianwei Niu, Hao Su, Xiting Liu, Weiwei Xu, Pei Lv, Bing Zhou, and Yi Yang. 2021. ART-UP: A novel method for generating scanning-robust aesthetic QR codes. *ACM Transactions on Multimedia Computing, Communications, and Applications (TOMM)* 17, 1 (2021), 1–23.
- Mingliang Xu, Hao Su, Yafei Li, Xi Li, Jing Liao, Jianwei Niu, Pei Lv, and Bing Zhou. 2019. Stylized Aesthetic QR Code. *IEEE Transactions on Multimedia* 21, 8 (2019), 1960–1970. <https://doi.org/10.1109/TMM.2019.2891420>
- Zhe Yang, Yuting Bao, Chuhan Luo, Xingya Zhao, Siyu Zhu, Chunyi Peng, Yunxin Liu, and Xinbing Wang. 2016. ARTcode: preserve art and code in any image. In *Proceedings of the 2016 ACM International Joint Conference on Pervasive and Ubiquitous Computing (Heidelberg, Germany) (UbiComp '16)*. Association for Computing Machinery, New York, NY, USA, 904–915. <https://doi.org/10.1145/2971648.2971733>
- Zhibo Yang, Huanle Xu, Jianyuan Deng, Chen Change Loy, and Wing Cheong Lau. 2018. Robust and Fast Decoding of High-Capacity Color QR Codes for Mobile Applications. *IEEE Transactions on Image Processing* 27, 12 (Dec. 2018), 6093–6108. <https://doi.org/10.1109/tip.2018.2855419>
- Guoxing Yu, Yongtao Hu, and Jingwen Dai. 2020. TopoTag: A robust and scalable topological fiducial marker system. *IEEE Transactions on Visualization and Computer Graphics* 27, 9 (2020), 3769–3780.

A A Bijection Between Natural Numbers and Bit Strings

While explaining the bit-tree encoding, we have modified the problem to work on natural numbers instead of bit strings, defining f' and g' so that:

$$\begin{aligned} f' : \mathbb{N} &\rightarrow \mathcal{T}, & g' : \mathcal{T} &\rightarrow \mathbb{N}, \\ f(b) &= f'(\text{nat}(b)) & g(T) &= \text{bits}(g'(T)) \end{aligned} \quad (12)$$

and assumed that the $\text{nat} : \{0, 1\}^* \rightarrow \mathbb{N}$ is a mapping from bit strings to natural numbers, while $\text{bits} : \mathbb{N} \rightarrow \{0, 1\}^*$ is its inverse. In the following, we present the bijection used in our implementation.

A simple mapping that converts a bit string $b = b_k b_{k-1} \dots b_1$ to a natural number n by treating it as the binary representation of n , i.e., $\text{nat}(b) = \sum_{i=0}^{k-1} b_{k-i} \cdot 2^i$, is not enough. In fact, if $b_k = 0$, then the function would map $b' = b_{k-1} \dots b_1$ to the same number as b , breaking the bijection. This problem can be avoided by appending a 1 to the input string, resulting in:

$$\text{nat}(b) = 2^{k+1} + \sum_{i=0}^{k-1} b_{k-i} \cdot 2^i \quad (13)$$

and its inverse $\text{bits}(n) = n_{\mathcal{B}}[1 :]$ where $n_{\mathcal{B}}$ is the binary string representation of n , and $[1 :]$ discards the first element of $n_{\mathcal{B}}$.

B Reduction of the Partitioning Minimization Problem to the Binary Case

The packer's partitioning minimization problem weighs circularity and area proportionality to produce a partitioning that increases scannability:

$$\min_{[P_1, \dots, P_k] \in \mathcal{P}} \sum_{i=1}^k \alpha |A(P_i) - A^*(P_i)| + (1 - \alpha) (1 - R(P_i)). \quad (14)$$

In our packer implementation, we reduce this to the binary case, and then implement an algorithm that finds a solution of eq. (14) by recursively applying the binary case. In the following, we prove the reduction to the binary case. First, we instantiate eq. (14) with only two polygons P_1 and P_2 :

$$\begin{aligned} \min_{[P_1, P_2] \in \mathcal{P}} & \alpha |A(P_1) - A^*(P_1)| + (1 - \alpha) (1 - R(P_1)) \\ & + \alpha |A(P_2) - A^*(P_2)| + (1 - \alpha) (1 - R(P_2)). \end{aligned} \quad (15)$$

Factoring α and $(1 - \alpha)$, we obtain:

$$\begin{aligned} \min_{[P_1, P_2] \in \mathcal{P}} & \alpha (|A(P_1) - A^*(P_1)| + |A(P_2) - A^*(P_2)|) + \\ & + (1 - \alpha) (2 - (R(P_1) + R(P_2))). \end{aligned} \quad (16)$$

Since $P = P_1 \cup P_2$ and $P_1 \cap P_2 = \emptyset$, then it holds that $A(P_2) = A(P) - A(P_1)$. Moreover, Since in the binary case,

$$\begin{aligned} A^*(P_2) &= A(P) \cdot \frac{F(T_2)}{F(T_1) + F(T_2)} \\ \implies A^*(P_2) &= A(P) \cdot \left(1 - \frac{F(T_1)}{F(T_1) + F(T_2)}\right) \\ \implies A^*(P_2) &= A(P) - A(P) \cdot \frac{F(T_1)}{F(T_1) + F(T_2)}. \end{aligned}$$

Then, $A^*(P_2) = A(P) - A^*(P_1)$. Therefore, we rewrite eq. (16):

$$\begin{aligned} \min_{[P_1, P_2] \in \mathcal{P}} & \alpha (|A(P_1) - A^*(P_1)| + |(A(P) - A(P_1)) - (A(P) - A^*(P_1))|) + \\ & + (1 - \alpha) (2 - (R(P_1) + R(P_2))). \end{aligned} \quad (17)$$

Which simplifies into:

$$\min_{[P_1, P_2] \in \mathcal{P}} 2\alpha (|A(P_1) - A^*(P_1)|) + (1 - \alpha) (2 - (R(P_1) + R(P_2))). \quad (18)$$

Finally, we divide by 2, obtaining the formulation:

$$\min_{[P_1, P_2] \in \mathcal{P}} \alpha |A(P_1) - w_1 A(P)| + (1 - \alpha) \left(1 - \frac{R(P_1) + R(P_2)}{2}\right) \quad (19)$$

where w_1 is $\frac{F(T_1)}{F(T_1) + F(T_2)}$.

C Contours Detection Algorithm

The algorithm scans the binary image row by row. When an unvisited foreground pixel (x, y) is encountered (i.e., $B(x, y) = 1$), it initiates the boundary tracing. The boundary is traced by iteratively exploring the 8-connected neighborhood:

$$N(x, y) = \{(x + i, y + j) \mid i, j \in \{-1, 0, 1\}, (i, j) \neq (0, 0)\}. \quad (20)$$

The boundary tracing process continues until the starting pixel is reached, forming a closed contour.

Each detected contour is stored as a sequence of points $\pi = \{p_1, p_2, \dots, p_k\}$, where $p_i = (x_i, y_i)$ represents the coordinates of the i -th pixel on the contour.

Contours are detected using a border-following technique on the binary image. Suzuki and Abe algorithm is used [Bradski 2000; Suzuki and Abe 1985] which efficiently detects contours and processes their hierarchy. The algorithm also organizes contours into a hierarchical structure, representing their nesting relationships. For each contour π_i , the hierarchy is described by a 4-tuple:

$$H[i] = [\text{Next}, \text{Previous}, \text{FirstChild}, \text{Parent}], \quad (21)$$

where **Next** is the index of the next contour at the same hierarchical level; **Previous** is the index of the previous contour at the same level; **FirstChild** is the index of the first child contour (nested within π_i); **Parent** is the index of the parent contour (enclosing π_i). The hierarchy is constructed by examining the spatial relationships between contours. A contour π_j is considered a child of π_i if all points of π_j lie within the boundary of π_i . This can be expressed mathematically as:

$$\forall (x, y) \in \pi_j, (x, y) \in \text{Interior}(\pi_i). \quad (22)$$

Here, $\text{Interior}(\pi_i)$ denotes the region enclosed by the contour π_i .

This hierarchical representation enables the scanner to reconstruct a comprehensive topological tree for the input image.